ELEMENTA
Science of the Anthropocene

Gabarró, C, et al. 2022. First results of the ARIEL L-band radiometer on the MOSAiC Arctic Expedition during the late summer and autumn period. *Elem Sci Anth*, 10: 1. DOI: https://doi.org/10.1525/elementa.2022.00031

RESEARCH ARTICLE

First results of the ARIEL L-band radiometer on the MOSAiC Arctic Expedition during the late summer and autumn period

Carolina Gabarró[1,*], Pau Fabregat[2], Ferran Hernández-Macià[1], Roger Jove[2], Joaquin Salvador[1], Gunnar Spreen[3], Linda Thielke[3], Ruzica Dadic[4], Marcus Huntemann[3], Nikolai Kolabutin[5], Daiki Nomura[6], Henna-Reetta Hannula[7], and Martin Schneebeli[8]

Arctic sea ice is changing rapidly. Its retreat significantly impacts Arctic heat fluxes, ocean currents, and ecology, warranting the continuous monitoring and tracking of changes to sea ice extent and thickness. L-band (1.4 GHz) microwave radiometry can measure sea ice thickness for thin ice $\leq$1 m, depending on salinity and temperature. The sensitivity to thin ice makes L-band measurements complementary to radar altimetry which can measure the thickness of thick ice with reasonable accuracy. During the Multidisciplinary drifting Observatory for the Study of Arctic Climate (MOSAiC) expedition, we deployed the mobile ARIEL L-band radiometer on the sea ice floe next to research vessel *Polarstern* to study the sensitivity of the L-band to different sea ice parameters (e.g., snow and ice thickness, ice salinity, ice and snow temperature), with the aim to help improve/validate current microwave emission models. Our results show that ARIEL is sensitive to different types of surfaces (ice, leads, and melt ponds) and to ice thickness up to 70 cm when the salinity of the sea ice is low. The measurements can be reproduced with the Burke emission model when in situ snow and ice measurements for the autumn transects were used as model input. The correlation coefficient for modeled Burke brightness temperature (BT) versus ARIEL measurements was approximately 0.8. The discrepancy between the measurements and the model is about 5%, depending on the transects analyzed. No explicit dependence on snow depth was detected. We present a qualitative analysis for thin ice observations on leads. We have demonstrated that the ARIEL radiometer is an excellent field instrument for quantifying the sensitivity of L-band radiometry to ice and snow parameters, leading to insights that can enhance sea ice thickness retrievals from L-band radiometer satellites (such as Soil Moisture Ocean Salinity (SMOS) and Soil Moisture Active Passive (SMAP)) and improve estimates of Arctic sea-ice thickness changes on a larger scale.

Keywords: Radiometry, Arctic, Emissivity, Sea ice, SMOS

1. Introduction

At low microwave frequencies (<2 GHz), electromagnetic waves penetrate tens of centimeters into the sea ice column (Heygster et al., 2014). This degree of penetration allows passive low-frequency radiometers to measure emissions from deeper within the ice than higher frequency radiometers, such as Advanced Microwave Scanning Radiometer-2 (AMSR-2). Therefore, the thickness of thin sea ice can be measured with these instruments. At L-band, 1.4 GHz, the sensitivity to ice thickness ranges between 50 cm and 1 m, but this range can increase, depending on salinity and temperature of the ice (Kaleschke et al., 2012; Maaß et al., 2013; Huntemann et al., 2014).

L-band radiometry is an excellent tool for monitoring Arctic sea ice thickness because, currently, 70% (in January) of the Arctic ice is seasonal and, therefore, thin ice (Kwok, 2018). Radar altimeters, the standard instrument to measure sea ice thickness, can only accurately measure ice thicker than approximately 1 m. Therefore, L-band radiometers and radar altimeters are complementary (Ricker et al., 2017b; data in webpage Ricker et al.,

[1] Barcelona Expert Center (BEC), Institute of Marine Science (ICM-CSIC), Barcelona, Spain
[2] Balamis—Microwave Sensors and Electronics Ltd, Barcelona, Spain
[3] Institute of Environmental Physics, University of Bremen, Bremen, Germany
[4] Victoria University of Wellington, Wellington, New Zealand
[5] Arctic and Antarctic Research Institute, St. Petersburg, Russia
[6] Hokkaido University, Hakodate, Japan
[7] Finnish Meteorological Institute, Helsinki, Finland
[8] WSL Institute for Snow and Avalanche Research SLF, Davos, Switzerland

* Corresponding author:
Email: cgabarro@icm.csic.es

2017a). However, while many altimeters have been measuring for more than three decades, few L-band radiometers are currently in operation: for example, the Soil Moisture and Ocean Salinity (SMOS) (Mecklenburg et al., 2009; Font et al., 2010; Kerr et al., 2010) the Soil Moisture Active Passive (SMAP) (Entekhabi et al., 2010) satellites, and the Federated Satellite System Catalan (FSSCAT) nanosatellite (Camps et al., 2018). There is much room for improvement for L-band inversion methods, emission models, dielectric models, and validation methodologies.

The SMOS (European Space Agency, ESA) and SMAP (National Aeronautics and Space Administration, NASA) missions provide unique and indispensable instruments to improve our knowledge of the critical climate variables such as sea ice thickness and volume. Since SMOS was launched in 2009, we have an almost 12-year series of sea ice thickness (SIT) maps (Tian-Kunze et al., 2014; Tian-Kunze and Kaleschke, 2021). Two future Copernicus Sentinel Expansion missions will carry L-band radiometers, e.g. CIMR (Copernicus Imaging Microwave Radiometer; Kilic et al., 2018), and will be launched soon.

Some inversion methods for retrieving sea ice thickness parameters from SMOS and SMAP use emission and dielectric constant models (Kaleschke et al., 2012). They are based, however, on limited instrumentation or obtained at other frequencies and then extrapolated to L-band. Therefore, revision and improvement of sea ice microwave emission models at the low microwave bands (in particular L-band, 1.4 GHz) are needed to improve satellite SIT retrieval.

The year-round (September 2019 to October 2020) Multidisciplinary drifting Observatory for the Study of Arctic Climate (MOSAiC) expedition offered an excellent opportunity to undertake measurements of sea ice parameters during a whole year (Nicolaus et al., 2022), providing the potential to study how the sea ice microwave emissivity signature changes with seasonal variability, with temperature variations and with the transition from melting to freezing periods.

During the MOSAiC campaign, we deployed a small and light radiometer called ARIEL, designed and developed at the Spanish company Balamis (https://www.balamis.com/). This portable radiometer was installed on a sledge and pulled by human operators along transects of variable length, allowing the acquisition of sea ice brightness temperatures under different sea ice conditions. Additionally, portable instruments acquired measurements of sea ice thickness (ground-based electromagnetic induction instrument, GEM) and snow depth (MagnaProbe and Snow Micro Penetrometer, SMP) in the same track as ARIEL during transect measurements. Here, we present the results of the ARIEL radiometer acquired during the end of August and September 2020 of the MOSAiC expedition and demonstrate the high capability of this 1.4 GHz radiometer to advance knowledge of the sensitivity of TB to ice and snow parameters.

2. Methods and approach

In September 2019, the German research icebreaker *Polarstern* departed from Tromsø, Norway, to spend a year drifting in the Arctic Ocean with the sea ice. The goal of the MOSAiC expedition was to examine, much more closely than ever before, the Arctic climate system as the epicenter of global warming and thus to gain fundamental insights that are key to a better understanding of global climate change (https://mosaic-expedition.org/) (Nicolaus et al., 2022). Here, we analyze ARIEL transect measurements performed on Leg 5 from August 30 to September 30, 2020.

2.1. Remote Sensing experimental setup

During the MOSAiC expedition, the 'Remote Sensing team' deployed several instruments on the ice similar to the payloads onboard satellites. The Remote Sensing site during Leg 5 was located around 88.2°N and 110°E (realize that the sea ice and therefore the instruments were moving); maps and more details are provided in Nicolaus et al. (2022) and Shupe et al. (2022). The objective was to develop new methods and algorithms to improve the current sea ice and snow parameters retrieval from satellites (e.g., ice concentration, sea ice thickness, and ice type), reducing and quantifying their uncertainties. Most of the measurements were performed in the microwave domain from 0.5 to 89 GHz using passive microwave radiometers and active radars (see **Figure 1a**). The instruments were co-deployed with simultaneous in situ snow and ice measurements, more details are provided in Nicolaus et al. (2022). The measurements were made both in a static position (at the Remote Sensing site) and by performing transects to study spatial variability and temporal evolution of TB. Here, we discuss the ARIEL radiometer deployments during transects only (between August 30 and September 30), and static observing leads. The sampling strategy of the transect measurements consisted of repeat surveys around 230 m in length. The transects were done on the main Central Observatory 3 (CO3) floe and on the return trip of the *Polarstern* to Germany, where three ice stations were performed, mainly in the marginal ice zone.

The objective of the ARIEL measurements was to understand better the sensitivity of the brightness temperatures at 1.4 GHz to ice and snow depth, snow density, temperature, and salinity of the ice and snow, among other parameters. Our results will pave the way to improving the satellite measurements of thin sea ice thickness performed with L-band radiometry.

2.2. ARIEL L-band radiometer

The ARIEL radiometer is a dual-polarization (H+V) total power radiometer with internal calibration. The central frequency is 1.41 GHz, with a bandwidth of 20 MHz. The system has a 2x1 patch antenna, with a beam width of 36° at 3 dB in the azimuth direction and 70° at 3 dB at the elevation angle. The radiometric accuracy of ARIEL is 1.06 K at a 1 Hz sampling frequency, with the capability to measure at higher sampling rates (up to 10 Hz)

Figure 1. Remote Sensing instruments used during MOSAiC. (a) All instruments used at the Remote Sensing site, (b) the ARIEL instrument during static measurements, and (c) ARIEL during transect measurements on the ice floe. Photo credits: Gunnar Spreen.

at the expense of the radiometric accuracy. A co-located thermal infrared photodiode to measure the surface temperature and a GPS receiver complete the sensor equipment. Calibration is performed with a hot load and a cold load (more information in Section 2.2.1). Here we refer to H- and V-polarization as H-pol and

V-pol, with corresponding brightness temperatures as TBH and TBV.

To adapt the ARIEL instrument to the harsh and cold conditions of the Arctic, we increased the internal thermal resistance by performing two modifications. The first modification was to add isolating material. The second was to apply a conformal coating to protect the electronics against humidity.

This light (7 kg) and small radiometer (40 cm x 60 cm x 20 cm) is ideal for frequent maneuvers. The radiometer was mounted on a wooden sledge to measure microwave emission at 40° incidence angle with respect to nadir (see **Figure 1**). This incidence angle is the operating angle from SMAP and is close to the 55° degree angle of the future CIMR mission and the AMSR-2 radiometer. SMOS has a multi-angular measuring system, from 0–60°, but at 40° the accuracy is higher than at other incidence angles (Zine et al., 2008). The radiometer was mounted at 1-m height with respect to the surface, so the ARIEL snapshot on the surface was 1.2 m in diameter.

From July to September 2020, ARIEL acquired good-quality measurements. Prior to July, a problem with the instrument hardware introduced too much noise, preventing the derivation of valid TB measurements. During those measurements, the ARIEL accuracy was 2.3 K (instead of 1 K) due to a software error on the sampling rate. The raw ARIEL data from that period can be downloaded in Gabarró et al. (2022b). During the last period of the expedition (from August 23 to September 30), forty-nine acquisitions were performed. Of those acquisitions, ten were transects, and the rest were static measurements at the Remote Sensing site or in a lead. Ten July acquisitions were also made between July 13 and July 26, four of which were transects.

The ARIEL operators carried out measurements in a static position, pointing the instrument to specific types of surfaces (thick ice, leads, rafted ice, melt ponds) and measuring different surface types at various stops (melt ponds, rafted ice, snow, etc.). Snow and surface scattering layer (SSL) height were also measured at the same locations.

The radiometer sledge was profiled along transects (about 230 m long) together with other sensors (such as MagnaProbe and GEM), thereby collating measurements of brightness temperatures with sea ice and snow depth thickness and other properties.

MagnaProbe provides direct snow depth measurements (Sturm and Holmgren, 2018), and GEM measures an induced secondary electromagnetic field in seawater, which allows estimating the ice-plus-snow thickness. Snow properties were measured in dedicated snow pits, and snow height was derived from SMP measurements along the transects.

2.2.1. ARIEL calibration and processing procedure

A calibration procedure for the radiometers is needed to convert the measured voltages to brightness temperatures. The calibration of ARIEL was done by pointing the radiometer to cold and hot targets. The cold target was the cold sky (approximate temperature of 6 K, Le Vine and Skou, 2006), while the hot target was absorber material at the instrument frequency stored in a large box with an emissivity of 1. The calibration was performed every 3–5 days.

Several corrections were performed to compensate for the large antenna beam width by taking into account the antenna radiation pattern. The following noise filtering techniques were also performed:

- We corrected for the sky contribution ($T_{sky} = 6\ K$) to compensate for the TB coming from the sky received by the top-front part of the antenna.
- We corrected for the co-polar and cross-polar radiation to compensate for the part of TB that comes from the other polarization (for more details see Fabregat, 2021).
- We considered that TB should be below the ice temperature measured with the infrared (IR) sensor because emissivity should be below 1 by definition.
- We discarded the measurements that differed more than 3 sigma ($3 * \sigma$) from the mean value of the sliding window of 100 samples.
- We discarded the points outside the quantile filter of 10%.

After filtering the outliers, the data were smoothed to reduce the noise further. Finally, a sliding window of 20 samples was applied, which has proven to work better with ARIEL data, reducing standard deviation (STD) and, therefore, the noise of the measurements (Fabregat, 2021).

Because the radiometer was used over a moving ice floe, the position with respect to the *Polarstern* was calculated, in addition to the GPS position, to simplify the co-location with other instrument measurements. We used a Python code provided by Dr. Stefan Hendricks (AWI) to compute this relative position (GitLab reference: https://gitlab.awi.de/floenavi-crs).

2.2.2. ARIEL measurement product output

The MOSAiC ARIEL data are available in netCDF format, being FAIR and netCDF compliant, through PANGAEA and the FTP server from the Barcelona Expert Center (BEC) webpage (http://bec.icm.csic.es). The ARIEL output from the MOSAiC expedition is available in two formats:

- ARIEL L0 data, which include ARIEL samples in voltages, calibration values, sea ice surface temperature, and the time and the GPS position, which can be downloaded from Gabarró et al. (2022b); and
- ARIEL L1 data, which include ARIEL TB in H and V polarization, sea ice surface temperature (acquired with the IR sensor), and the GPS and relative position to *Polarstern*.

The processing procedure is presented in the BEC technical note (Gabarró et al., 2021).

2.2.3. ARIEL transects and weather conditions

ARIEL operators repeated seven transects along the same path during the measurement period. The meteorological conditions during the transects can be found in **Table 1**,

Table 1. Dates and weather conditions of the MOSAiC ARIEL transects from late August through September 2020

Date	ARIEL Measure Code	Air Temperature (°C)[a]	Weather Conditions
Main ice floe CO3			
Aug 30	59-376	−0.60	After melting period, wet ice
Aug 31	60-9	−0.75	Small ice pellets precipitated
Sep 3	60-79	−0.64	Freezing conditions for 3 days, melt ponds still open, 2-cm snow depth
Sep 7	61-58	−3.41	Freezing, windy with snow the previous days, all ponds frozen, drifting snow, wet snow and ice
Sep 10	60-145	−7.90	Freezing conditions with light snow grains falling (approximately 7-cm snow depth), melt ponds frozen
Sep 14	61-14	−2.53	Melting conditions with rain, mist, and strong gusts in the morning
Sep 17	60-104	−6.26	Snow drifts, 2-cm snow depth on top of crust layer
Departing ice floe			
Sep 24	63-38	−0.85	Wet snow, some pooling with higher salinity, windy and cloudy
Sep 26	63-70	−5.07	New snow, calm and cloudy, snowing later in the day
Sep 30	63-242	−6.09	Drifted and wind-packed snow, windy

[a]Obtained from the 2-m height sensor on the Meteorological tower (Shupe et al., 2022).

along with weather conditions from visual observations. The transects were performed in two sets:

- The first set of transects was done between August 30 and September 17 on the main MOSAiC ice floe CO3. That floe was mainly second-year ice, which had just survived the second summer after partial melting and associated brine loss. These transects were repeated on different days, permitting the study of the variation and sensitivity of TB to changes in the ice, snow, and melt ponds.
- The second set of transects was performed after leaving the main summer floe during the return to Germany. The team performed measurements at three ice stations on three different ice floes, on September 24, 26, and 30. These transects were conducted mainly on thinner and more homogeneous level ice, mainly first and second-year ice.

2.3. Ancillary in situ measurements

Simultaneously with ARIEL measurements, other equipment acquired data to characterize the ice and snow properties near the radiometric measurements, as described below. An overview of the ice and snow in situ and the remote sensing measurements is given in Nicolaus et al. (2022).

2.3.1. Ice thickness and snow depth in situ measurements

A ground-based electromagnetic induction sensor (Geophex GEM-2) was used to measure the combined ice and snow/SSL thickness continuously during each transect. The GEM was mounted on a plastic sledge and pulled along, following other instruments. The average accuracy of GEM-2 was about 10 cm (Stefan Hendricks, personal communication) during the analyzed period. For details on the data processing, handling and accuracy, we refer to Haas and Eicken (2001) and Hunkeler et al. (2016).

Thermal emission from snow is small at low microwave frequencies because its attenuation is negligible. However, it still impacts both the ice temperature and the refraction of sea ice emissions. The snow depth measurements accompanying the MagnaProbe were carried out with an automated snow/SSL depth probe (Snow Hydro MagnaProbe). Unfortunately, these measurements were not in the same position as ARIEL stops, so we have not used these data in the following analysis.

We used the snow depth data measured with the SMP at each stop. SMP provides (Proksch et al., 2015) a fast retrieval of the vertical profile of snow stratigraphy, snow density, and specific surface area, with a high vertical resolution (better than 1 mm). For this study, we used only snow height retrievals from SMP. At each ARIEL stop, repeated SMP measurements were taken adjacent to or directly on the ARIEL footprint. During the CO3 transects and on September 24, 5 measurements were repeated within a 1-m distance. During the last two transects (September 26 and 30), 18 measurements were repeated on a grid of 5 x 1.5 m. If only five measurements were available, they are given the average. If 18 measurements were available, they are given as the average with STD.

These GEM-2 and SMP measurements followed the ARIEL path, permitting us to use the data as ground truth. Furthermore, snow pits measurements were performed at

Table 2. Date and sampling area, mean values with standard deviation (STD) for temperature and salinity, and ice thickness from MOSAiC ice cores collected in late August through September 2020

		Temperature (°C)		Salinity		
Date	Area[a]	Mean	STD	Mean	STD	Core Length (cm)
Main ice floe CO3						
Aug 29	Strength area	−0.40	0.34	1.28	0.96	125
Aug 31	Main area	−0.51	0.45	2.10	1.21	148
Sep 7	Main area	−0.82	0.42	2.07	0.98	151
Sep 10	Strength area	−1.39	0.68	1.46	1.16	135
Sep 14	Main area	−0.60	0.43	1.67	1.48	162
Sep 17	Strength area	−1.35	0.54	–	–	141
Departing ice floe						
Sep 24	Ice station, second-year ice	−0.94	1.24	1.03	0.50	55
Sep 24	Ice station, young ice	−1.48	0.31	2.28	2.54	28
Sep 26	Ice station, second-year ice	−1.35	1.08	1.90	1.16	70
Sep 30	Ice station, second-year ice	−2.02	1.06	3.04	1.45	50

[a]More details about the area can be found in Nicolaus et al. (2022).

the beginning of most transects. The snow pits provide snow depth, temperature, salinity, density, permittivity, and microstructure.

2.3.2. Salinity and temperature profiles

Weekly ice cores were taken during MOSAiC, obtaining information on temperature and salinity profiles. However, the ice coring was not done at the same position as the ARIEL measurements. Here, we assume that the ice and snow salinity and temperature were spatially homogeneous on the MOSAiC ice floe. Ice coring on the main ice floe was close to a ridge, and the ice thickness at the Remote Sensing site (where ARIEL was measuring) was lower. During the last two transects on the departing ice floe, ARIEL measurements and the ice cores were taken on similar ice types and ice depths.

Table 2 shows the mean values with STD for temperature and salinity from the values of the ice cores during the analyzed period. Ice core depths were between 140 and 175 cm. The ice core data show low salinity during the period of interest in the CO3 ice floe (less than 2.2), which agrees with expected low salinity for older, multiyear ice (Eicken et al., 1995). The ice cores from the two ice floes visited during ice stations on the way back to Germany show higher salinity and lower ice temperatures, especially on September 30, when the snow cover was thicker and drier than at the previous stations.

2.4. Sea ice emission model at L-band

Emission models are crucial to understanding TB measurements and deriving sea ice parameters. To compare the brightness temperature measured with the L-band radiometer ARIEL, we have considered the Burke model (Burke et al., 1979) with four layers: air, snow, ice, and water.

The modeled emissivity of sea ice strongly depends on the electromagnetic properties of these layers. This model assumes that these layers are homogeneous, with a smooth surface. It also considers an isotropic sky brightness temperature of 6 K, with no absorption or attenuation between the surface and the sensor.

The ice and snow layers are assumed homogeneous and neglect volume scattering, as air bubbles and brine pockets are much smaller than the wavelengths at 1.4 GHz (21 cm). According to the empirical formula, modeled sea-ice dielectric properties are based on the brine volume fraction (Vant et al., 1978) and depend on the ice temperature and bulk salinity. The brine volume fraction is obtained from the Leppäranta and Manninen (1998) coefficients for $T_{ice} \geq -2^{\circ}\mathrm{C}$, and from the Cox and Weeks (1983) coefficients for $T_{ice} < -2^{\circ}\mathrm{C}$, assuming the density of pure ice after Pounder (1965). The permittivity of the snow, which has a significant impact on emission, is derived from Mätzler (1996), and the imaginary part from Tiuri et al. (1984) and Mätzler (2006). Lastly, the permittivity of the seawater is modeled using the Klein and Swift (1977) equations. The water layer is modeled as semi-infinite, and we used the following values: $T_w = -1.8^{\circ}\mathrm{C}$ and $S_w = 35$. The Burke model is largely insensitive to snow depth (<1 K), but it is sensitive to the presence of snow (especially on H-pol TB). Therefore, we have considered a snow thickness layer of 10% of the ice layer (Doronin, 1971) with a density of $\rho_s = 250$ kg m^{-3}, which is a typical value for September in the Arctic (Warren et al., 1999; Maaß et al., 2013). Although there may not always be snow cover but the surface scattering layer instead, the

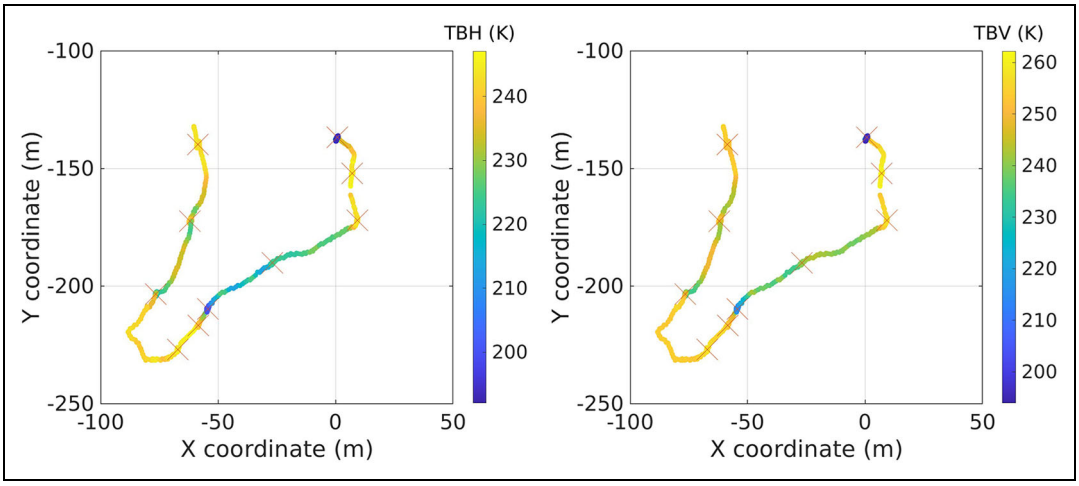

Figure 2. ARIEL transect taken on the MOSAiC CO3 ice floe on September 3, 2020. This transect of brightness temperatures by H-polarization (TBH, left) and V-polarization (TBV, right) was performed on September 3, with ten stops. X and Y coordinates indicate meter distances with respect to the *Polarstern*. The color scale bars indicate the TBH and TBV values.

density variation between the two surfaces does not impact the modeled brightness temperature significantly. For the temperature and the salinity of the ice (T_{ice} and S_{ice}), we computed the mean value of the ice core measurements (see **Table 2**). We assumed an isothermal snowpack with the same temperature as the mean value of the ice. We further assumed that T_{ice} and S_{ice} were spatially homogeneous on the MOSAiC floe, because the ice cores were taken in the vicinity but not next to ARIEL (Nicolaus et al., 2022).

3. Results

3.1. Transect measurements

During the CO3 transects, ten stops of 3–5 minutes each were performed to acquire radiometric measurements in a static position to avoid tilting and shaking the instrument due to surface inhomogeneities. The stops were performed during repeated transects on the MOSAiC CO3 ice floe, at the same positions for all transects. **Figure 2** shows the transect track with respect to the *Polarstern* reference frame (axis in meters) from September 3.

Figure 3 shows the TB during transects of August 30 and September 17, both along the same track. The surface temperature obtained from the ARIEL IR sensor is plotted over the TB. The ten stops are marked on the plots. During stops number 6 and 10, the ARIEL pointed to melt ponds (see photos in **Figure 4**), with stop 10 being a large melt pond (**Figure 4c** and **d**). On August 30, the IR temperature sensor recorded a mean surface temperature of 0.6°C at all stops except at stop 10, where it recorded 0.7°C. On September 17, most stops recorded values between –4.1 and –4.2°C, except stops 6 and 10, when a temperature of –3.4°C was recorded, which might indicate that the ice was thinner, as expected over a refrozen meltpond. We observed an increase in the mean TB of both polarizations for the September 17 transect, which is expected

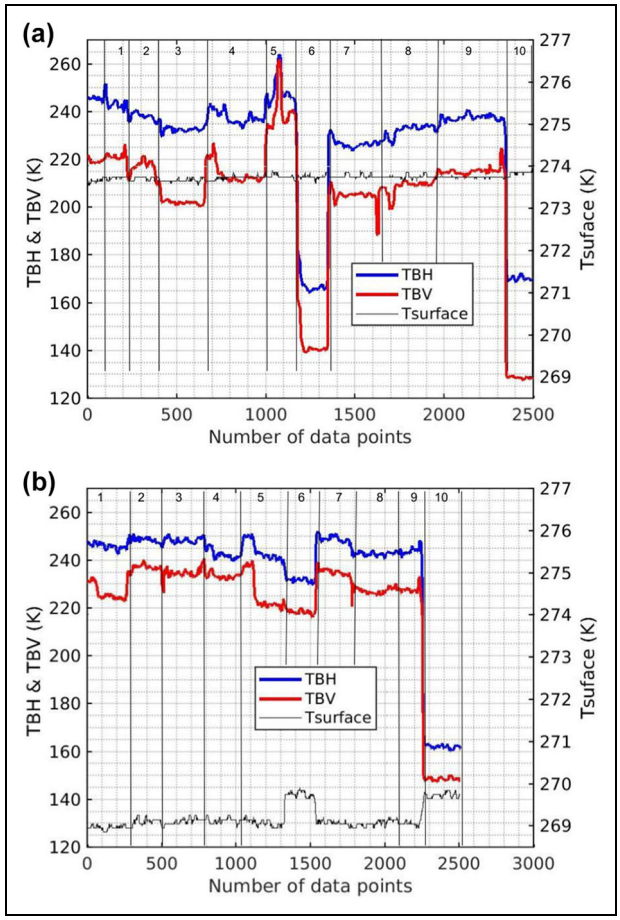

Figure 3. ARIEL brightness temperatures during transects on the MOSAiC CO3 ice floe. Brightness temperatures by H-polarization (TBH) and V-polarization (TBV) are shown for transects on (a) August 30 and (b) September 17, along with measurements of surface temperature from ARIEL (Tsurf).

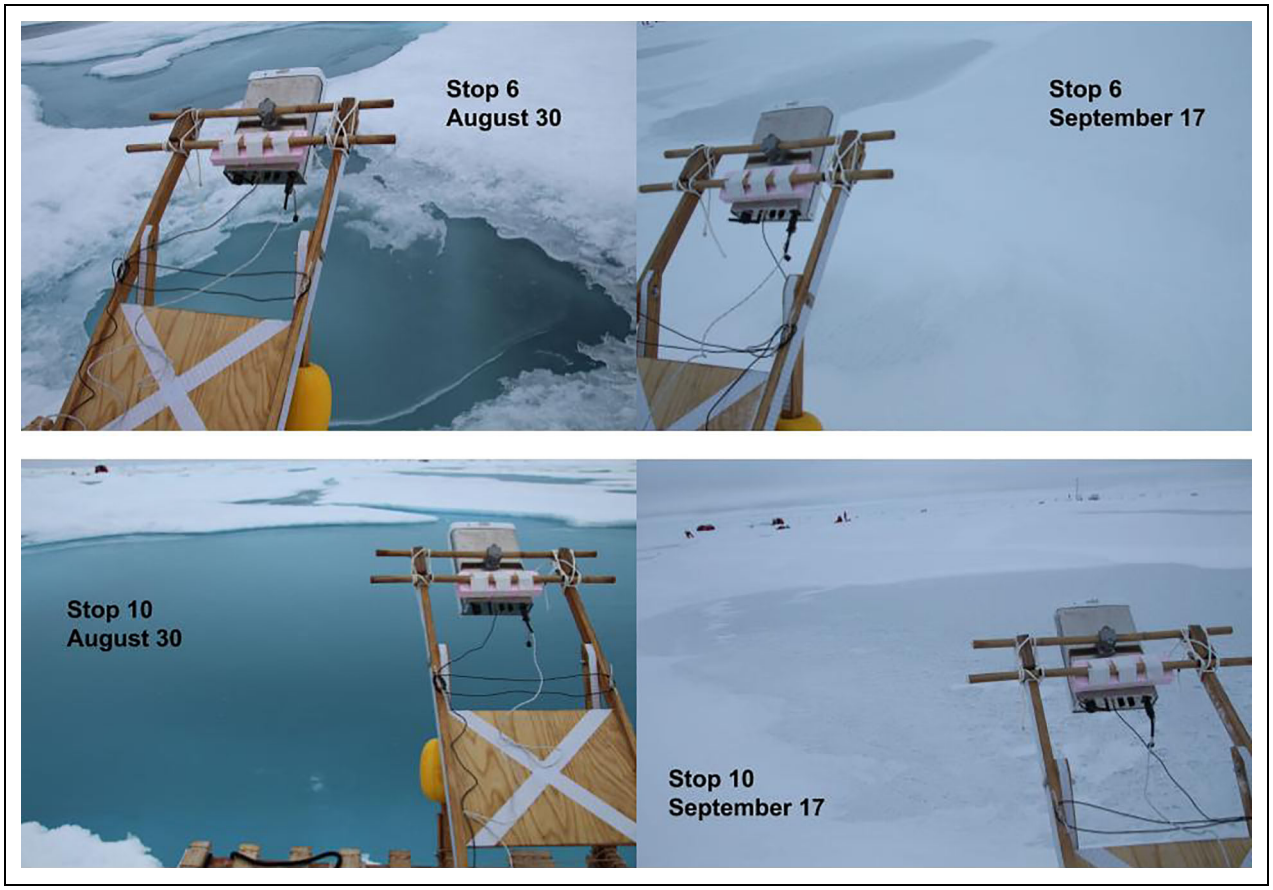

Figure 4. Photographs of ARIEL measuring melt ponds on MOSAiC transects on the CO3 ice floe. Images of stop 6 (top) and stop 10 (bottom) along transects on August 30 (left) and September 17 (right). Note the formation of a thin ice cover on the melt pond at stop 10 between August 30 and September 17. Photo credits: Linda Thielke.

as TB increases with colder and thicker ice. On September 17, the melt pond at stop number 6 was frozen and snow-covered, which caused an increase in the TB (see **Figure 4**), making the values more similar to the rest of the transect. There is almost no increase in TB at stop number 10 on September 17. This large melt pond was covered by very thin ice, which is clearly discernible in the photograph in **Figure 4d**. However, there is a slight increase in TBH, but not TBV, which we cannot explain. We expected an increase of both polarizations for a thin ice layer.

3.1.1. Sensitivity to ice thickness

We computed the median value of the TB measurements acquired at each stop (between 120 and 180 measurements per stop) and co-located them with each transect's GEM sea ice thickness measurements. We also computed the STD of TB per stop. We omitted the measurements where the STD was larger than 10 K, those with a surface temperature of the infrared sensor above 274 K, and those where TBH was larger than TBV because those measurements were not representative of the analysis we performed below. In addition, we omitted measurements of melt ponds because we did not have co-located GEM measurements and did not know the ice thickness.

The TB sensitivity to SIT depends mainly on the salinity and temperature of the ice and can vary considerably (Vant et al., 1978; Kaleschke et al., 2012; Huntemann, 2015). Low ice salinity and high ice temperature produce less brine volume and, therefore, less signal loss, i.e. thicker ice becomes "visible." **Figure 5** shows the median value of TB at each stop as a function of the ice thickness during the transects on September 3, 7, 10, and 17.

The Burke model brightness temperatures were computed using the boundary conditions discussed in Section 2.4 as input. We computed the average value for salinity and temperature from ice cores extracted during the period of interest (September 7, 10, 14, and 17; **Table 2**) to compute the TB model. We dismissed the measurements from August 29 and 31 because the air temperature was above zero, so the ice was wet and the model is not valid for wet conditions. The values used in the model are $T_{ice} = -1.18°C$ (STD = 0.31°C; days September 7, 10, 14 and 17) and $S_{ice} = 1.73$ (STD = 0.31; only days September 7, 10 and 14, because we do not have salinity measurements on September 17). The model results are shown in **Figure 5** (dashed black line). The blue lines show modeled TB using maximum and minimum salinity and temperature from ice cores. These model results show that the small variability of T_{ice} and S_{ice} during the analyzed period

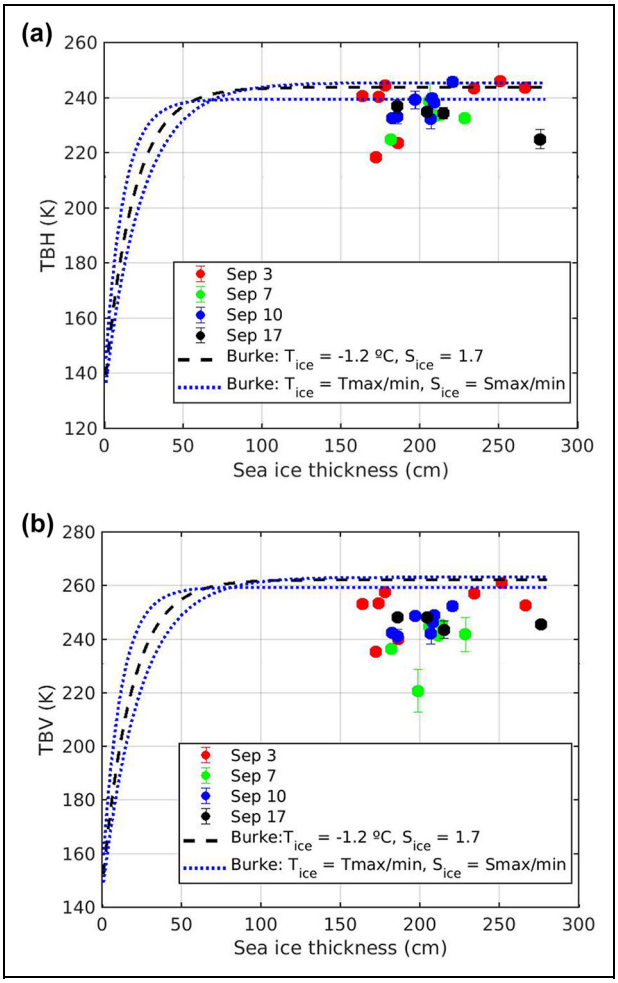

Figure 5. ARIEL TB sensitivity to sea ice thickness on the MOSAiC CO3 ice floe. Observed brightness temperatures by (a) H-polarization (TBH) and (b) V-polarization (TBV) as a function of ice thickness from ground-based electromagnetic (GEM) measurements during transects on September 3, 7, 10, and 17. The Burke model brightness temperatures, using $S_{ice} = 1.73$ and $T_{ice} = -1.18$°C as model input, are plotted with dashed black lines. Dotted blue lines show modeled TB using T_{ice} max and min (−0.82 and −1.39°C) and S_{ice} max and min (2.07 and 1.46) from the different ice cores. The error bars represent the STD of the measurements at each stop.

(14 days) has a negligible impact on modeled TBs for thick ice (more than 100 cm). For this study, we can thus use an average T_{ice} and S_{ice} as model input.

We emphasize that the measurements were made on ice thicker than 1.5 m, and therefore outside the expected TB sensitivity to SIT (Kaleschke et al., 2012; Huntemann et al., 2014). Modeled TB is sensitive to SIT up to 70 cm (dashed line in **Figure 5**). For our observed brightness temperatures (on thicker ice), the model has a bias and does not fit the measurements.

We hypothesize that these discrepancies between model and measurements may be due to horizontal heterogeneity in the ice area observed by the radiometer, where completely undisturbed level ice was sparse. Even though ARIEL was pointing at ice areas that appeared to be homogeneous on top, the ice beneath may have had high porosity or large cavities due to the close-by small ridges and melt ponds. Moreover, we assumed a single bulk sea ice salinity in the emission modeling. This assumption may not be correct, because the ice floe was second-year ice with some melting and refreezing events, such that two or three sea ice layers with different salt concentrations would improve the modeled TB, as in Demir et al. (2022). In the future, we will consider modeling each transect with a more detailed set of parameters (instead of averaging ice core data over four weeks) to improve temporal representation of the model.

Figure 6a and **b** show the TBH and TBV with respect to ice thickness for the three transects carried out during the ice stations after departing the CO3 ice floe (September 24, 26, and 30). During these three transects, the ice was thinner than the CO3 ice. Therefore, TB measurements show larger variability and sensitivity to ice thickness. In addition, the acquisitions during the stops were longer during the transects (more TB data points), which reduced the noise.

We ran the Burke model with the values stated in Section 2.4 and salinity and temperature ice values of $S_{ice} = 2.35$, $T_{ice} = -1.47$°C (average value from ice cores in **Table 2**). The measurements from September 26 are noisy, but in general, the Burke model shows good agreement with measured TBs. Neither modeled nor measured TB show a dependence on SIT above 70 cm. The range of model input (T_{ice} and S_{ice}) from available ice cores during the period of interest (**Table 2**) shows little variation in modeled TB (blue lines in **Figures 5** and **6**).

Figure 6c and **d** are scatter plots between model output and ARIEL measurements for H-pol and V-pol and show high correlations (0.83 for H-pol and 0.74 for V-pol). The correlations are statistically significant because the off-diagonal values of the p-values matrix are lower than a significance level of 0.05; i.e. $1.77e-7$ for TBH and $4.02e-10$ for TBV.

3.1.2. Sensitivity to snow depth

Maaß et al. (2015) reported that, for cold Arctic conditions, the brightness temperature increases with increasing snow thickness. They explained that the TB dependence on snow thickness is due to the thermal insulation of snow, which is a function of snow thickness. When air temperatures are low, the snow acts as an insulator, causing a large temperature gradient between the surface and the snow-ice interface.

The conditions for the analyzed period (end of summer) differed from those described in Maaß et al. (2015) because the air temperature was only a few degrees below zero (**Table 1**). The average temperature difference between the snow surface and the snow-ice interface was less than 3.5°C for all the transects. The snow surface and interface temperatures were measured with a handheld thermometer.

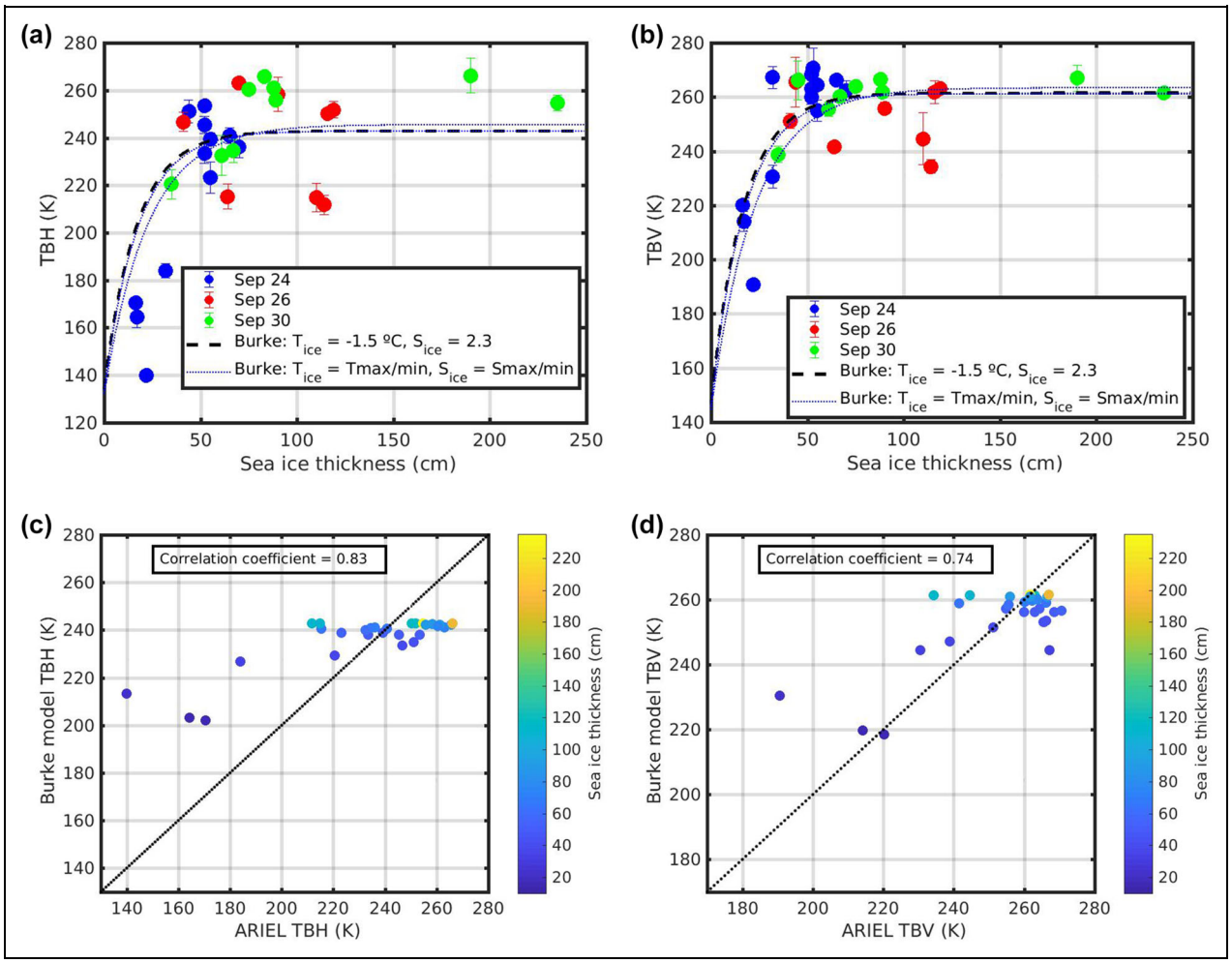

Figure 6. TB sensitivity to sea ice thickness on transects during the return of *Polarstern*. Observed brightness temperatures by (a) H-polarization (TBH) and (b) V-polarization (TBV) as a function of sea ice thickness (SIT). The Burke model results used salinity and temperature from ice cores as input ($S_{ice} = 2.35$, $T_{ice} = -1.47°C$). Blue lines show modeled TB with T_{ice} max and min (−2.02 and −0.94°C) and S_{ice} max and min (3.4 and 0.50) from different ice cores. Panels (c) and (d) show scatter plots between Burke model output and ARIEL measurements of (c) TBH and (d) TBV.

We show the dependence of TB on snow depth in **Figure 7**. We used snow depth data obtained from SMP in the same (or nearby) ARIEL location for each stop. We did not use the MagnaProbe data because the measurements were not made at the exact ARIEL locations.

The analysis shows no clear dependence of TB on snow depth. We assume that this result is due to the small temperature gradient between the surface and snow-ice interface (less than 3.5°C). Another possible reason is that the range of snow depth observations is small (3 cm to 12 cm) compared with other studies (Maaß et al., 2015). More measurements during the winter period with larger gradients between the surface and the snow-ice interface temperature and a greater range of snow thicknesses are needed to verify the dependence of TB on snow depth as described in Maaß et al. (2015).

3.1.3. Error assessment with respect to the model

The mean, STD, root mean squared (RSM), and mean relative error of the measurements and the model results are shown in **Table 3**, where a mean ice salinity and the temperature has been used for each set of transects, as explained in Section 3.1.1. The STD and RMS of the measured TB versus modeled TB for the departing ice floe transects (September 24, 26, and 30) are larger than for the CO3 transects (September 3, 7, 10, and 17). This difference is due to the larger TB variability (120 K) for the departing transects than for the CO3 transects (40 K). The mean value and relative error, however, are smaller for the departing transects, indicating a lower bias on the measurements.

These errors could be due to multiple sources and because we made many generalized assumptions, such as:

- Ice cores: The salinity and temperature of the ice were neither determined at the location of the ARIEL measurements nor on the same days. The available data do not allow us to account for the likely temporal and spatial variability due to ridging and melt ponds during the summer

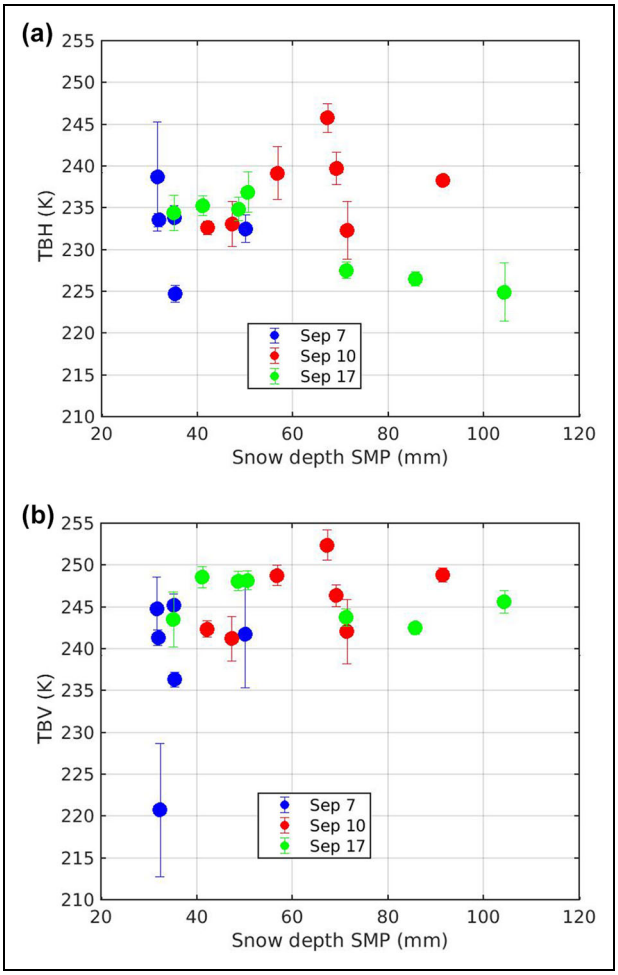

Figure 7. TB sensitivity to snow depth on the MOSAiC CO3 ice floe. Observed brightness temperatures by (a) H-polarization (TBH) and (b) V-polarization (TBV) as a function of snow depth measured with Snow Micro Penetrometer (SMP) for three transects on September 7, 10, and 17. Error bars of TB are the standard deviation of the measurements per stop; with only 5 SMP measurements per stop during these transects, so this statistic is not representative.

period. The maximum vertical variability in available ice cores was approximately 4°C for temperature, and approximately 5 for salinity. Therefore, the model simplification of using a single ice layer with uniform salinity and temperature may be a source of model uncertainties.

- Sea ice thickness from GEM: The GEM SIT measurements we used are preliminarily processed data (not finally processed). However, as we were working on relatively level sea ice, we assumed an uncertainty of 10 cm (Stefan Hendricks, personal communication).
- ARIEL uncertainty: As explained earlier, the ARIEL precision is 2.3 K.
- ARIEL incidence angle (inclination): The structure to support the ARIEL on the sledge is made of wood and may not have an exact 40° incidence angle. Moreover, because the ice is not flat, the sled could cause a larger inclination than expected. For an error of 5° in the incidence angle, we expect a TB variation of approximately 3–5 K (depending on the SIT, T_{ice}, and S_{ice}, among other parameters).

Given the potentially large sources of errors, as expected during a field campaign, the results are encouraging.

3.2. Temporal evolution of freezing leads

Several measurements were made over a lead, by pointing the radiometer at the lead, to monitor the evolution of thin ice on leads during freezing. During summer melt, the MOSAiC ocean team reported a prominent freshwater lens under sea ice and in leads (Rabe et al., 2022), but this freshwater lens was not detected after the freeze onset. We used the atmospheric observations from a nearby met-tower at the 2-m level and weather observations to link the observed brightness temperature changes to changes in atmospheric conditions.

We studied the evolution of a lead using ARIEL measurements from September 10 to September 19, a period

Table 3. Mean, standard deviation (STD), root mean squared (RMS), mean relative error[a] and correlation coefficient between ARIEL measurements and Burke model output

Correlation Tested[b]	Mean	STD	RMS	Relative Error (%)	Correlation Coefficient
Main ice floe September 3, 7, 10, and 17					
TBH_obs versus TBH_mod	−8.15	7.32	10.86	−3.55	–
TBV_obs versus TBV_mod	−16.26	8.37	18.21	−6.73	–
Departing ice floe September 24, 26, and 30					
TBH_obs versus TBH_mod	−3.52	23.84	23.68	−3.25	0.83
TBV_obs versus TBV_mod	−0.18	12.66	12.45	−0.11	0.74

[a]Relative error = (TB-TB_mod)/TB*100.

[b]Brightness temperatures observed by H-polarization (TBH_obs) and V-polarization (TBV_obs) versus modeled TB (TBH_mod and TBV_mod).

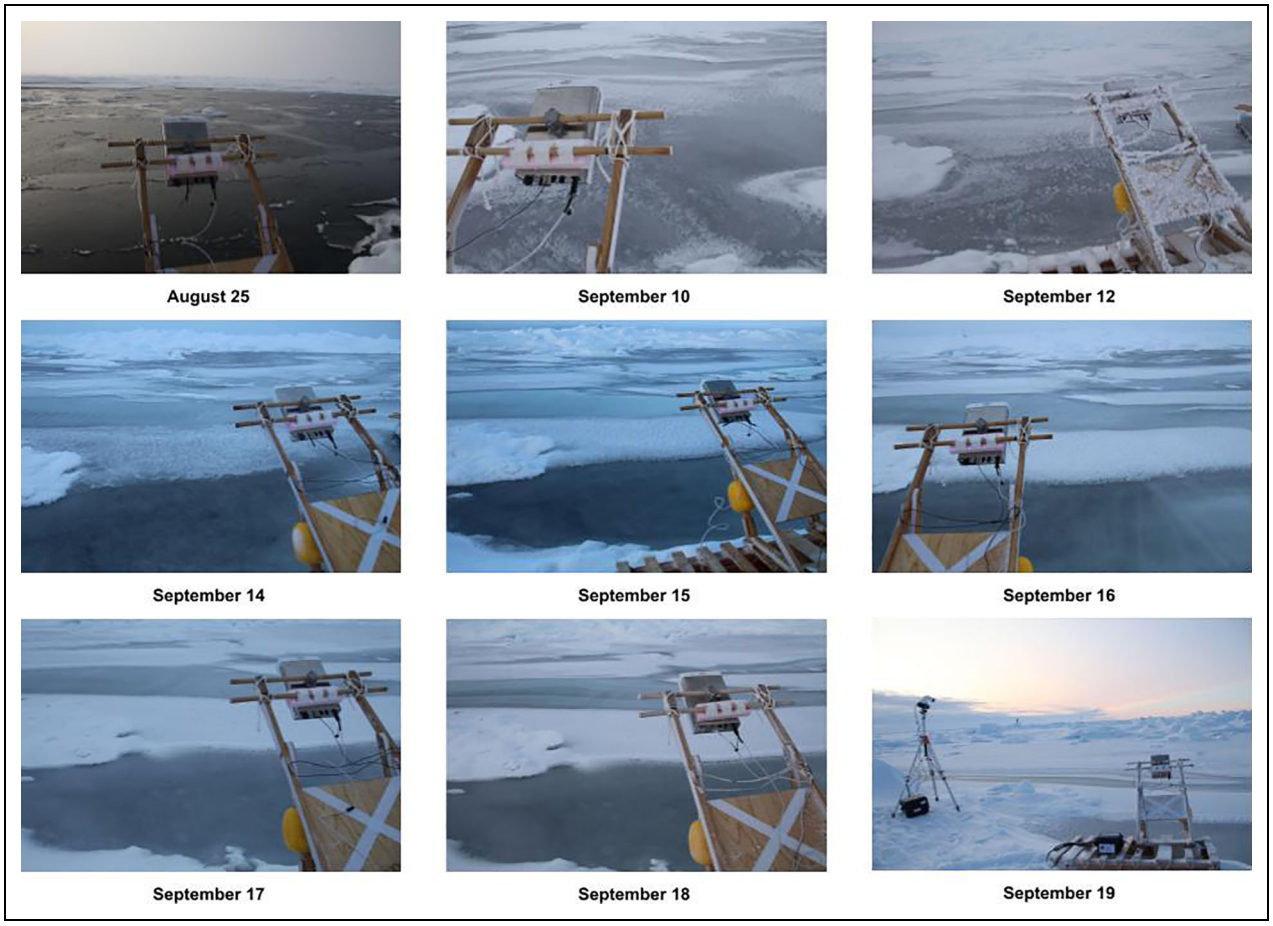

Figure 8. ARIEL measurements being made while pointed over leads. Pictures of the radiometer observing the lead at the Remote Sensing site from August 25 (top left) to September 19 (bottom right). Photo credits: Linda Thielke.

Table 4. Information on the status of the lead at the MOSAiC Remote Sensing site in September 2020

		Lead Water		Feature Thickness (cm)		
Date	Air (2-m) Temperature (°C)	Temperature (°C)	Salinity	Ice	Freeboard	Slush
Sep 10	−7.90	−1.9	27.9	8	–	0
Sep 12	−6.76	−1.6	26.7	14	4	–[a]
Sep 14	−2.53	–	–	–	–	–[b]
Sep 15	−4.67	–	–	–	–	–
Sep 16	−4.39	–	–	–	–	–
Sep 17	−6.25	−2.1	23.0	20	0	1
Sep 18	−9.03	–	–	–	–	–
Sep 19	−3.31	−1.3	23.0	22	0	1

[a]Small topographic change observed in the ice, with some hoar frost but no snow on the ice surface.

[b]Some water observed on ice, after melting and rain.

during which the ice thickness on the lead changed considerably (**Figure 8a**). ARIEL measurements were performed for approximately 20 hours every day, with a gap on September 11 and September 13. Air temperature, sea ice thickness and the lead water properties for the period of interest are summarized in **Table 4**.

Figure 9 shows the brightness temperature of the lead evolution from September 10 to 19 (TBH and TBV, in blue and red, respectively). The surface temperature (Tsurf) from the ARIEL IR sensor (green line) and the 2-m air temperature (Tair, black line) are over-plotted (Shupe et al., 2022). The high TB variability is due to active ice

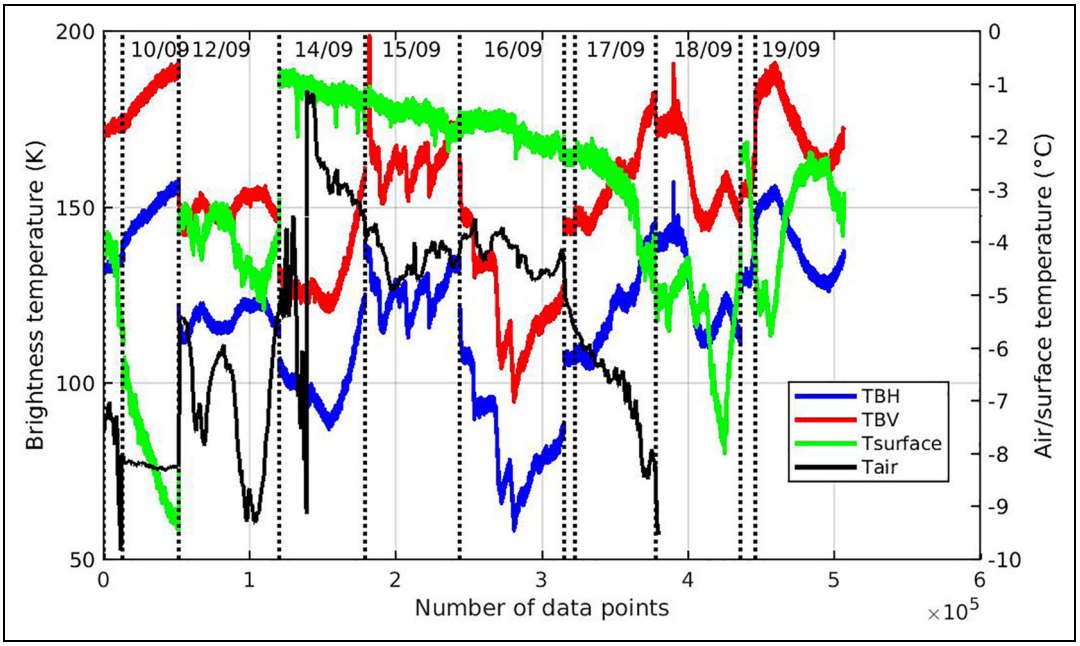

Figure 9. ARIEL brightness temperatures over a lead at the Remote Sensing site. Observed brightness temperatures by H-polarization (TBH, blue line) and V-polarization (TBV, red line) at the Remote Sensing site lead from September 10 to September 19 (date format on figure is day/month). Surface ice (Tsurf) and 2-m air (Tair) temperatures (Schmithüsen et al., 2021) are over plotted. The dotted vertical lines indicate different measured days.

dynamics and the changing ice and weather conditions. The ice growth in the lead was not homogeneous, and the lead was very dynamic. Ice was rafted, with lateral opening and partial closing (see **Figure 8**).

The conclusions derived from the lead analysis are mainly qualitative because we do not have enough data on the thickness of newly formed sea ice (see **Table 4**). Moreover, ARIEL's broad field of view causes the measured TB to be an integration of the TB emitted by the lead plus the TB emitted by the surrounding sea ice, making a partially frozen lead difficult to analyze before the lead is completely frozen (starting on September 17).

Atmospheric observations documented in the MOSAiC Cruise Report from Leg 5 (team ice) show that the above-freezing conditions at the end of August and at the beginning of September did not favor new ice growth. The freezing started on September 3, and continued until September 13. This process can be observed in **Figure 8** top pictures, where the lead started to form new ice on August 25, although a first consistent ice layer over the lead was not observed until September 10. On September 13 and 14, atmospheric conditions changed from freezing to above-freezing. Moreover, rain fell on September 13 and September 14, adding puddles of rainwater, meltwater and light snow accumulation on top of the lead. This change is reflected in the TB decrease on September 14 (red and blue lines in **Figure 9**).

On September 14 towards the evening, the air temperature dropped and caused the onset of refreezing, which is reflected in the sudden increase of retrieved TB (**Figure 9**). The signal in both TBs then undulates on September 15, which we cannot explain. Perhaps the wind changed, causing lead dynamics and ice movement, which then affected TBs. A further drop in air temperature on September 16 caused the ice on the lead to freeze, leading to more homogeneous ice growth and a clear increase in TBs.

4. Conclusions

The light portable ARIEL L-band radiometer successfully acquired data on the ice on the MOSAiC expedition during autumn 2020. The radiometric measurements (brightness temperature) fell within the expected range for sea ice. ARIEL measurements were co-located with ground truth data, such as GEM sea ice thickness and SMP snow depth measurements. Although ARIEL also acquired data during July 2020, this period was not considered here in order to focus on data acquired only during transects.

The analysis described in this paper shows that ARIEL TB is sensitive to ice thickness up to approximately 70 cm. Furthermore, a clear correlation between TB and sea ice thickness was observed on the autumn transects performed on thinner ice.

We compared the ARIEL measurements with a four-layer model following Burke et al. (1979). For the first set of transects (beginning of September, on the MOSAiC CO3 ice floe), the model output does not fit with radiometric measurements when using a single ice layer with the ice salinity and temperature obtained from ice core data averaged over four weeks. This lack of fit might be because the ice cover was heterogeneous along the transect, with small ridges (which may contain cavities and are more porous than the level sea ice), melt ponds, and snow/SSL variability, so that only in small areas was typical level ice present. This ice heterogeneity could have influenced the ARIEL measurements, preventing a match to the simplified model output (which considers homogeneous level

ice). Also, using one value for salinity and one for temperature is not likely valid.

The second set of transects (during three ice stations after departing the CO3 ice floe) was conducted on a thinner and more homogeneous level ice floe, and therefore the range of measured TB was larger (as expected from the model). Comparing these ARIEL brightness temperatures and the Burke model run using ice core measurements as input showed a good correlation, with correlation coefficients of 0.83 for TBH and 0.74 for TBV. The sensitivity of TB to snow depth was also analyzed, but we found no clear relationship within the temperature and snow thickness ranges encountered during this period of the campaign.

The radiometer also made measurements over a lead for 8 days. The TB measurements largely reflect the reported ice thickness and weather conditions (freezing/melting), but our analysis of this aspect was entirely qualitative for lack of sufficient data.

We have been able to show that the ARIEL radiometer is sensitive to variations in SIT below 70 cm, for the analyzed ice conditions. ARIEL is also an excellent instrument for field campaigns, thanks to its lightweight and simplicity of operation. However, further analysis should be done with more advanced emission models using more sea ice layers, as in Demir et al. (2022). In-situ drilling of the sea ice to get exact thickness would be helpful to address GEM-2 measurement uncertainties.

We highly recommend acquiring more field measurements, and combining the ARIEL radiometer with in situ measurements (ground truth) during the Arctic autumn and winter periods, especially when ice grows, as no measurements were made for these seasons during MOSAiC. Furthermore, a more detailed analysis of the dependence of TB on snow depth and density needs to be undertaken, which will require more co-located data. New field data would permit continued analyses for validating and improving the current sea ice emission models at L-band.

Data accessibility statement

All of the data used in this study are included in **Tables 1** and **2** of this manuscript and are available from the PANGAEA webpage (Gabarró et al., 2022a; Gabarró et al., 2022b). The data are also available on the Barcelona Expert Center webpage (https://bec.icm.csic.es/).

Acknowledgments

We acknowledge the Spanish Funding Agency (AEI) for funding the Programación Conjunta Internacional project called ICE-MOD PCI2019-111844-2. This work was carried out and data used in this manuscript were produced as part of the Multidisciplinary drifting Observatory for the Study of Arctic Climate (MOSAiC) with the tag MOSAiC20192020. We thank all persons involved in the expedition of the research vessel *Polarstern* during MOSAiC in 2019–2020 (AWI_PS122_00; as listed in Nixdorf et al., 2021). We also thank all Leg 5 ice and snow team for taking detailed measurements and Steffan Hendricks for the GEM data and for helping to interpret them. We would also like to thank the ice core, snow, transect, and ECO team: Mats Granskog, Marc Oggier, Allison Fong, Emelia Chamberlain, Elise Droste, Ulrike Dietrich, Alison Webb, Marcel Nicolaus, Julia Regnery, Roberta Pirazzini, Jan Rohde, and Melinda Webster. We thank Justino Martinez for his help in the preparatory work of the field campaign. This work is part of the CSIC Interdisciplinary Thematic Platforms (PTI): Teledetección (PTI-TELEDETECT) and (PTI) Polar zone Observatory (PTI-POLARCSIC). This work acknowledges the "Severo Ochoa Centre of Excellence" accreditation (CEX2019-000928-S).

Funding

This study and resulting paper have been done thanks to the Spanish funding Agency (AEI), who funded the Programación Conjunta Internacional project called "MEJORANDO LOS MODELOS DE EMISIVIDAD DEL HIELO MARINO EN LAS MICROONDAS DE BAJA FRECUENCIA" (ICE-MOD), with reference PCI2019-111844-2. GS and MH is supported by the Deutsche Forschungsgemeinschaft in the framework of the MOSAiCmicrowaveRS project (grant 420499875). GS and CG acknowledge support from the European Union's Horizon 2020 research and innovation program under grant agreement no. 101003826 via project CRiceS (Climate Relevant interactions and feedbacks: the key role of sea ice and snow in the polar and global climate system).

Competing interests

The authors have no competing interests.

Author contributions

Contributed to conception and design: CG, FH-M, RD, GS.

Contributed to acquisition of data: GS, LT, RD, H-RH, NK.

Contributed to preparing the instrument for the field campaign: JS, CG.

Contributed to processing the radiometric data: CG, PF, RJ, FH-M.

Contributed to analysis and interpretation of data: All authors.

Drafted and/or revised the article: All authors.

Approved the submitted version for publication: All authors.

References

Burke, W, **Schmugge, T**, **Paris, J.** 1979. Comparison of 2.8- and 21-cm microwave radiometer observations over soils with emission model calculations. *Journal of Geophysical Research* **84**: 287–294. DOI: http://dx.doi.org/10.1029/JC084iC01p00287.

Camps, A, **Golkar, A**, **Gutierrez, A**, **de Azua, JR**, **Munoz-Martin, J**, **Fernandez, L**, **Diez, C**, **Aguilella, A**, **Briatore, S**, **Akhtyamov, R**, **Garzaniti, N.** 2018. Fsscat, the 2017 Copernicus Masters' "Esa Sentinel Small Satellite Challenge" Winner: A federated polar and soil moisture tandem mission based on 6U Cubesats. *IGARSS 2018–2018 IEEE International Geoscience and Remote Sensing Symposium*: 8285–8287. DOI: http://dx.doi.org/10.1109/IGARSS.2018.8518405.

Cox, G, **Weeks, W.** 1983. Equations for determining the gas and brine volumes in sea-ice samples. *Journal of Glaciology* **29**(102): 306–316.

Demir, O, **Johnson, JT**, **Jezek, KC**, **Andrews, MJ**, **Ayotte, K**, **Spreen, G**, **Hendricks, S**, **Kaleschke, L**, **Oggier, M**, **Granskog, MA**, **Fong, A**, **Hoppmann, M**, **Matero, I**, **Scholz, D.** 2022. Measurements of 540–1740 MHz brightness temperatures of sea ice during the winter of the MOSAiC campaign. *IEEE Transactions on Geoscience and Remote Sensing* **60**: 1–11. DOI: http://dx.doi.org/10.1109/TGRS.2021.3105360.

Doronin, Y. 1971. *Thermal interaction of the atmosphere and the hydrosphere in the Arctic*. Philadelphia, PA: CoronetBooks.

Eicken, H, **Lensu, M**, **Leppäranta, M**, **Tucker, W**, **Gow, A**, **Salmela, O.** 1995. Thickness, structure, and properties of level summer multiyear ice in the Eurasian sector of the Arctic Ocean. *Journal of Geophysical Research* **1002**: 22697–22710. DOI: http://dx.doi.org10.1029/95JC02188.

Entekhabi, D, **Njoku, EG**, **O'Neill, PE**, **Kellogg, KH**, **Crow, WT**, **Edelstein, WN**, **Entin, JK**, **Goodman, SD**, **Jackson, TJ**, **Johnson, J**, **Kimball, J**, **Piepmeier, JR**, **Koster, RD**, **Martin, N**, **McDonald, KC**, **Moghaddam, M**, **Moran, S**, **Reichle, R**, **Shi, JC**, **Spencer, MW**, **Thurman, SW**, **Tsang, L**, **Van Zyl, J**. 2010. The soil moisture active passive (SMAP) mission. *Proceedings of the IEEE* **98**(5): 704–716.

Fabregat, P. 2021. L-band radiometry: Data processing and emissivity models for Arctic sea-ice [Bachelor's degree in Telecommunications Technologies and Services]. Barcelona, Spain: Universitat Politecnica de Catalunya.

Font, J, **Camps, A**, **Borges, A**, **Martin-Neira, M**, **Boutin, J**, **Reul, N**, **Kerr, Y**, **Hahne, A**, **Mecklenburg, S.** 2010. SMOS: The challenging sea surface salinity measurement from space. *Proceedings of the IEEE* **98**(5): 649 –665. DOI: http://dx.doi.org/10.1109/JPROC.2009.2033096.

Gabarró, C, **Fabregat, P**, **Hernández-Macià, F**, **Spreen, G**, **Thielke, L.** 2022a. Brightness temperature measured by ARIEL radiometer at 1.4 GHz from July to September 2020 during the MOSAiC expedition. *PANGAEA, Raw horizontal and vertical polarization voltages from the L-band BALAMIS ARIEL radiometer acquired during the MOSAiC expedition (Leg 4 and 5)*. DOI: http://dx.doi.org10.1594/PANGAEA.943755.

Gabarró, C, **Fabregat, P**, **Team, B.** 2021. *ARIEL on MOSAIC expedition products description*. Barcelona, Spain: BEC, ICM-CSIC.

Gabarró, C, **Jove, R**, **Salvador, J**, **Hernández-Macià, F**, **Martnez, J**, **Spreen, G**, **Thielke, L**, **von Albedyll, L.** 2022b. Raw horizontal and vertical polarization voltages from the L-band BALAMIS ARIEL radiometer acquired during the MOSAiC expedition (Leg 4 and 5). *PANGAEA*. DOI: http://dx.doi.org/10.1594/PANGAEA.942958.

Haas, C, **Eicken, H.** 2001. Interannual variability of summer sea ice thickness in the Siberian and central Arctic under different atmospheric circulation regimes. *Journal of Geophysical Research: Oceans* **106**(C3): 4449–4462. DOI: http://dx.doi.org/10.1029/1999JC000088; https://agupubs.onlinelibrary.wiley.com/doi/abs/10.1029/1999JC000088.

Heygster, G, **Huntemann, M**, **Ivanova, N**, **Saldo, R**, **Pedersen, LT.** 2014. Response of passive microwave sea ice concentration algorithms to thin ice. *2014 IEEE Geoscience and Remote Sensing Symposium*: 3618–3621. DOI: http://dx.doi.org/10.1109/IGARSS.2014.6947266.

Hunkeler, PA, **Hoppmann, M**, **Hendricks, S**, **Kalscheuer, T**, **Gerdes, R.** 2016. A glimpse beneath Antarctic Sea ice: Platelet layer volume from multi-frequency electromagnetic induction sounding. *Geophysical Research Letters* **43**(1): 222–231. DOI: http://dx.doi.org/10.1002/2015GL065074; https://agupubs.onlinelibrary.wiley.com/doi/abs/10.1002/2015GL065074.

Huntemann, M. 2015. Thickness retrieval and emissivity modeling of thin sea ice at L-band for SMOS satellite observations [Ph.D. thesis; doctoral dissertation]. Bremen, Germany: Staats-und Universitätsbibliothek.

Huntemann, M, **Heygster, G**, **Kaleschke, L**, **Krumpen, T**, **Mäkynen, M**, **Drusch, M.** 2014. Empirical sea ice thickness retrieval during the freeze-up period from SMOS high incident angle observations. *The Cryosphere* **8**: 439–451. DOI: http://dx.doi.org/10.5194/tc-8-439-2014.

Kaleschke, L, **Tian-Kunze, X**, **Maaß, N**, **Mäkynen, M**, **Drusch, M.** 2012. Sea ice thickness retrieval from SMOS brightness temperatures during the Arctic freeze-up period. *Geophysical Research Letters* **39**(5). DOI: http://dx.doi.org/101029/2012GL050916.

Kerr, Y, **Waldteufel, P**, **Wigneron, J**, **Delwart, S**, **Cabot, F**, **Boutin, J**, **Escorihuela, M**, **Font, J**, **Reul, N**, **Gruhier, C**, **Juglea, S**, **Drinkwater, M**, **Hahne, A**, **Martin-Neira, M**, **Mecklenburg, S.** 2010. The SMOS mission: New tool for monitoring key elements of the global water cycle. *Proceedings of the IEEE IGARSS 2010, no 5* **98**: 666–687.

Kilic, L, **Prigent, C**, **Aires, F**, **Boutin, J**, **Heygster, G**, **Tonboe, RT**, **Roquet, H**, **Jimenez, C**, **Donlon, C.** 2018. Expected performances of the Copernicus imaging microwave radiometer (CIMR) for an all-weather and high spatial resolution estimation of ocean and sea ice parameters. *Journal of Geophysical Research: Oceans* **123**(10): 7564–7580. DOI: http://dx.doi.org/10.1029/2018JC014408; https://agupubs.onlinelibrary.wiley.com/doi/abs/10.1029/2018JC014408.

Klein, L, **Swift, C**. 1977. An improved model for the dielectric constant of sea water at microwave frequencies. *IEEE Transactions on Antennas and Propagation* **AP-25**(1): 104–111.

Kwok, R. 2018. Arctic sea ice thickness, volume, and multiyear ice coverage: Losses and coupled variability (1958–2018). *Environmental Research Letters* **13**(10): 105005. DOI: http://dx.doi.org/10.1088/1748-9326/aae3ec.

Le Vine, D, **Skou, N**. 2006. *Microwave radiometer systems: Design and analysis*. 2nd ed. Norwood, MA: Artech House.

Leppäranta, M, **Manninen, T**. 1998. The brine and gas contents of sea-ice with attention to low salinities and high temperatures. Finnish Institute of Marine Research. Internal Report 2. Available at http://hdl.handle.net/1834/23905.

Maaß, N, **Kaleschke, L**, **Tian-Kunze, X**, **Drusch, M.** 2013. Snow thickness retrieval over thick Arctic Sea ice using SMOS satellite data. *The Cryosphere* **7**(6): 1971–1989. DOI: http://dx.doi.org10.5194/tc-7-1971-2013; https://tc.copernicus.org/articles/7/1971/2013/.

Maaß, N, **Kaleschke, L**, **Tian-Kunze, X**, **Tonboe, RT.** 2015. Snow thickness retrieval from L-band brightness temperatures: A model comparison. *Annals of Glaciology* **56**(69). DOI: http://dx.doi.org/10.3189/2015AoG69A886.

Mätzler, C. 1996. Microwave permittivity of dry snow. *IEEE Transactions on Geoscience and Remote Sensing* **34**(2): 573–581. DOI: http://dx.doi.org/10.1109/36.485133.

Mätzler, C. 2006. *Thermal microwave radiation: Applications for remote sensing*. London, UK: Institution of Electrical Engineers.

Mecklenburg, S, **Wright, N**, **Bouzina, C**, **Delwart, S.** 2009. Getting down to business—SMOS operations and products. *ESA Bulletin* **137**: 25–30.

Nicolaus, M, **Perovich, DK**, **Spreen, G**, **Granskog, MA**, **von Albedyll, L**, **Angelopoulos, M**, **Anhaus, P**, **Arndt, S**, **Belter, HJ**, **Bessonov, V**, **Birnbaum, G**, **Brauchle, J**, **Calmer, R**, **Cardellach, E**, **Cheng, B**, **Clemens-Sewall, D**, **Dadic, R**, **Damm, E**, **de Boer, G**, **Demir, O**, **Dethloff, K**, **Divine, DV**, **Fong, AA**, **Fons, S**, **Frey, MM**, **Fuchs, N**, **Gabarró, C**, **Gerland, S**, **Goessling, HF**, **Gradinger, R**, **Haapala, J**, **Haas, C**, **Hamilton, J**, **Henna-Reetta, H**, **Hendricks, S**, **Herber, A**, **Heuzé, C**, **Hoppmann, M**, **Høyland, KV**, **Huntemann, M**, **Hutchings, JK**, **Hwang, B**, **Itkin, P**, **Hans-Werner, J**, **Jaggi, M**, **Jutila, A**, **Kaleschke, L**, **Katlein, C**, **Kolabutin, N**, **Krampe, D**, **Kristensen, SS**, **Krumpen, T**, **Kurtz, N**, **Lampert, A**, **Lange, BA**, **Lei, R**, **Light, B**, **Linhardt, F**, **Liston, GE**, **Loose, B**, **Macfarlane, AR**, **Mahmud, M**, **Matero, IO**, **Maus, S**, **Morgenstern, A**, **Naderpour, R**, **Nandan, V**, **Niubom, A**, **Oggier, M**, **Oppelt, N**, **Pätzold, F**, **Perron, C**, **Petrovsky, T**, **Pirazzini, R**, **Polashenski, C**, **Rabe, B**, **Raphael, IA**, **Regnery, J**, **Rex, M**, **Ricker, R**, **Riemann-Campe, K**, **Rinke, A**, **Rohde, J**, **Salganik, E**, **Scharien, RK**, **Schiller, M**, **Schneebeli, M**, **Semmling, M**, **Shimanchuk, E**, **Shupe, MD**, **Smith, MM**, **Smolyanitsky, V**, **Sokolov, V**, **Stanton, T**, **Stroeve, J**, **Thielke, L**, **Timofeeva, A**, **Tonboe, RT**, **Tavri, A**, **Tsamados, M**, **Wagner, DN**, **Watkins, D**, **Webster, M**, **Wendisch, M**. 2022. Overview of the MOSAiC expedition: Snow and sea ice. *Elementa: Science of the Anthropocene* **10**(1). DOI: http://dx.doi.org/10.1525/elementa.2021.000046.000046.

Nixdorf, U, **Dethloff, K**, **Rex, SM**, **Shupe, M**, **Sommerfeld, A**, **Perovich, DK**, **Nicolaus, M**, **Heuze, C**, **Rabe, B**, **Loose, B**, **Damm, E**, **Gradinger, R**, **Fong, A**, **Maslowski, W**, **Rinke, A**, **Kwok, R**, **Spreen, G**, **Wendisch, M**, **Herber, A**, **Hirsekorn, M**, **Mohaupt, V**, **Frickenhaus, S**, **Immerz, A**, **Weiss-Tuider, K**, **Koenig, B**, **Mengedoht, D**, **Regnery, J**, **Gerchow, P**, **Ransby, D**, **Krumpen, T**, **Morgenstern, A**, **Haas, C**, **Kanzow, T**, **Rack, F**, **Saitzev, V**, **Sokolov, V**, **Makarov, A**, **Schwarze, S**, **Wunderlick, T**, **Wurr, K**, **Boetius, A**. 2021. *MOSAiC extended acknowledgement*. Zenodo. DOI: http://dx.doi.org/10.5281/zenodo.5541624.

Pounder, E. 1965. *The physics of ice*. Oxford, UK: Pergamon Press.

Proksch, M, **Löwe, H**, **Schneebeli, M**. 2015. Density, specific surface area, and correlation length of snow measured by high-resolution penetrometry. *Journal of Geophysical Research: Earth Surface* **120**: 346–362. DOI: http://doi.org/10.1002/2014JF003266.

Rabe, B, **Heuzé, C**, **Regnery, J**, **Aksenov, Y**, **Allerholt, J**, **Athanase, M**, **Bai, Y**, **Basque, C**, **Bauch, D**, **Baumann, TM**, **Chen, D**, **Cole, ST**, **Craw, L**, **Davies, A**, **Damm, E**, **Dethloff, K**, **Divine, DV**, **Doglioni, F**, **Ebert, F**, **Fang, YC**, **Fer, I**, **Fong, AA**, **Gradinger, R**, **Granskog, MA**, **Graupner, R**, **Haas, C**, **He, H**, **He, Y**, **Hoppmann, M**, **Janout, M**, **Kadko, D**, **Kanzow, T**, **Karam, S**, **Kawaguchi, Y**, **Koenig, Z**, **Kong, B**, **Krishfield, RA**, **Krumpen, T**, **Kuhlmey, D**, **Kuznetsov, I**, **Lan, M**, **Laukert, G**, **Lei, R**, **Li, T**, **Torres-Valdés, S**, **Lin, L**, **Lin, L**, **Liu, H**, **Liu, N**, **Loose, B**, **Ma, X**, **McKay, R**, **Mallet, M**, **Mallett, RDC**, **Maslowski, W**, **Mertens, C**, **Mohrholz, V**, **Muilwijk, M**, **Nicolaus, M**, **O'Brien, JK**, **Perovich, D**, **Ren, J**, **Rex, M**, **Ribeiro, N**, **Rinke, A**, **Schaffer, J**, **Schuffenhauer, I**, **Schulz, K**, **Shupe, MD**, **Shaw, W**, **Sokolov, V**, **Sommerfeld, A**, **Spreen, G**, **Stanton, T**, **Stephens, M**, **Su, J**, **Sukhikh, N**, **Sundfjord, A**, **Thomisch, K**, **Tippenhauer, S**, **Toole, JM**, **Vredenborg, M**, **Walter, M**, **Wang, H**, **Wang, L**, **Wang, Y**, **Wendisch, M**, **Zhao, J**, **Zhou, M**, **Zhu, J**. 2022. Overview of the MOSAiC expedition: Physical oceanography. *Elementa: Science of the Anthropocene* **10**(1). DOI: http://dx.doi.org/10.1525/elementa.2021.

Ricker, R, **Hendricks, S**, **Kaleschke, L**, **Tian-Kunze, X**, **King, J**, **Haas, C**. 2017a. SMOS & CryoSat-2 sea ice data product processing and dissemination service. Available at https://spaces.awi.de/pages/viewpage.action?pageId=291898639.

Ricker, R, **Hendricks, S**, **Kaleschke, L**, **Tian-Kunze, X**, **King, J**, **Haas, C**. 2017b. A weekly Arctic sea-ice thickness data record from merged CryoSat-2 and SMOS satellite data. *The Cryosphere* **11**(4): 1607–1623. DOI: http://dx.doi.org/10.5194/tc-11-1607-2017; https://tc.copernicus.org/articles/11/1607/2017/.

Schmithüsen, H, **Raeke, A**, **Wenzel, J**. 2021. Meteorological observations during POLARSTERN cruise PS122/5. DOI: http://dx.doi.org10.1594/PANGAEA.935267.

Shupe, MD, **Rex, M**, **Blomquist, B**, **Persson, POG**, **Schmale, J**, **Uttal, T**, **Althausen, D**, **Angot, H**, **Archer, S**, **Bariteau, L**, **Beck, I**, **Bilberry, J**, **Bucci, S**, **Buck, C**, **Boyer, M**, **Brasseur, Z**, **Brooks, IM**, **Calmer, R**, **Cassano, J**, **Castro, V**, **Chu, D**, **Costa, D**, **Cox, CJ**, **Creamean, J**, **Crewell, S**, **Dahlke, S**, **Damm, E**, **de Boer, G**, **Deckelmann, H**, **Dethloff, K**, **Dütsch, M**, **Ebell, K**, **Ehrlich, A**, **Ellis, J**, **Engelmann, R**, **Fong, AA**, **Frey, MM**, **Gallagher, MR**, **Ganzeveld, L**, **Gradinger, R**, **Graeser, J**, **Greenamyer, V**, **Griesche, H**, **Griffiths, S**, **Hamilton, J**, **Heinemann, G**, **Helmig, D**, **Herber, A**, **Heuzé, C**, **Hofer, J**, **Houchens, T**, **Howard, D**, **Inoue, J**, **Jacobi, HW**, **Jaiser, R**, **Jokinen, T**, **Jourdan, O**, **Jozef, G**, **King, W**, **Kirchgaessner, A**, **Klingebiel, M**, **Krassovski, M**, **Krumpen, T**, **Lampert, A**, **Landing, W**, **Laurila, T**, **Lawrence, D**, **Lonardi, M**, **Loose, B**, **Lüpkes, C**, **Maahn, M**, **Macke, A**, **Maslowski, W**, **Marsay, C**, **Maturilli, M**, **Mech, M**, **Morris, S**, **Moser, M**, **Nicolaus, M**, **Ortega, P**, **Osborn, J**, **Pätzold, F**, **Perovich, DK**, **Petäjä, T**, **Pilz, C**, **Pirazzini, R**, **Posman, K**, **Powers, H**, **Pratt, KA**, **Preußer, A**, **Quéléver, L**, **Radenz, M**, **Rabe, B**, **Rinke, A**, **Sachs, T**, **Schulz, A**, **Siebert, H**, **Silva, T**, **Solomon, A**, **Sommerfeld, A**, **Spreen, G**, **Stephens, M**, **Stohl, A**, **Svensson, G**, **Uin, J**, **Viegas, J**, **Voigt, C**, **von der Gathen, P**, **Wehner, B**, **Welker, JM**, **Wendisch, M**, **Werner, M**, **Xie, Z**, **Yue, F**. 2022. Overview of the MOSAiC expedition: Atmosphere. *Elementa: Science of the Anthropocene* **10**(1). DOI: http://dx.doi.org/10.1525/elementa.2021.00060.

Sturm, M, **Holmgren, J**. 2018. An automatic snow depth probe for field validation campaigns. *Water Resources Research* **54**: 9695–9701. DOI: https://doi.org/10.1029/2018WR023559.

Tian-Kunze, X, **Kaleschke, L**. 2021. SMOS sea ice thickness data product processing and dissemination service. Available at https://spaces.awi.de/pages/viewpage.action?pageId=291898639.

Tian-Kunze, X, **Kaleschke, L**, **Maaß, N**, **Mäkynen, M**, **Serra, N**, **Drusch, M**, **Krumpen, T**. 2014. SMOS-derived thin sea ice thickness: Algorithm baseline, product specifications and initial verification. *The Cryosphere* **8**(3): 997–1018. DOI: http://dx.doi.org/10.5194/tc-8-997-2014; https://tc.copernicus.org/articles/8/997/2014/.

Tiuri, M, **Sihvola, A**, **Nyfors, E**, **Hallikaiken, M**. 1984. The complex dielectric constant of snow at microwave frequencies. *IEEE Journal of Oceanic Engineering* **9**(5): 377–382. DOI: http://dx.doi.org/10.1109/JOE.1984.1145645.

Vant, M, **Ramseier, R**, **Makios, V**. 1978. The complex-dielectric constant of sea ice at frequencies in the range 0.1–40 GHz. *Journal of Applied Physics* **49**: 1264–1280.

Warren, S, **Rigor, I**, **Untersteiner, N**, **Radionov, VF**, **Bryazgin, NN**, **Aleksandrov, Y**, **Colony, R**. 1999. Snow depth on arctic sea ice. *Journal of Climate* **12**(6): 1814–1829. DOI: http://dx.doi.org/10.1175/1520-0442(1999)012<1814:SDOASI>2.0.CO;2; https://journals.ametsoc.org/view/journals/clim/12/6/1520-0442_1999_012_1814_sdoasi_2.0.co_2.xml.

Zine, S, **Boutin, J**, **Font, J**, **Reul, N**, **Waldteufel, P**, **Gabarro, C**, **Tenerelli, J**, **Petitcolin, F**, **Vergely, J**, **Talone, M**, **Delwart, S**. 2008. Overview of the SMOS sea surface salinity prototype processor. *IEEE Transactions on Geoscience and Remote Sensing* **46**(3): 621–645. DOI: http://dx.doi.org/10.1109/TGRS.2008.915543.

How to cite this article: Gabarró, C, Fabregat, P, Hernández-Macià, F, Jove, R, Salvador, J, Spreen, G, Thielke, L, Dadic, R, Huntemann, M, Kolabutin, N, Nomura, D, Hannula, H-R, Schneebeli, M. 2022. First results of the ARIEL L-band radiometer on the MOSAiC Arctic Expedition during the late summer and autumn period. *Elementa: Science of the Anthropocene* 10(1). DOI: https://doi.org/10.1525/elementa.2022.00031

Domain Editor-in-Chief: Jody W. Deming, University of Washington, Seattle, WA, USA

Guest Editor: Marcel Nicolaus, Alfred-Wegener-Institut Helmholtz-Zentrum für Polar- und Meeresforschung, Bremerhaven, Germany

Knowledge Domain: Ocean Science

Part of an Elementa Special Feature: The Multidisciplinary Drifting Observatory for the Study of Arctic Climate (MOSAiC)

Published: September 23, 2022 **Accepted:** August 14, 2022 **Submitted:** February 18, 2022